

A multi-scale molecular dynamics study of the assembly of micron-size supraparticles from 30 nm alkyl-coated nanoparticles†

Cite this: *Phys. Chem. Chem. Phys.*, 2013, **15**, 8132

Damien Thompson,^{*a} Mateusz Sikora,^b Piotr Szymczak^c and Marek Cieplak^b

Atomistic and meso scale computer simulations of nanoparticle aggregation are combined to describe the self-assembly of supraparticles in bulk and on surfaces under vacuum conditions. At the nano scale, atomic resolution molecular dynamics simulations provide the structures of 30 nm-diameter nanoparticles bound to each other and to coated hydrophobic surfaces, through the physical contacting of their alkyl coats. This “molecular velcro” has been recently exploited in experiments to direct the aggregation of coated nanoparticles into stable assemblies on electronics platforms. Interaction potentials are extracted from the nano scale simulations and transferred to coarse grained Brownian dynamics simulations that describe multi-nanoparticle aggregation and surface deposition. The simulation results show that the large interaction area between 30 nm nanoparticles provides a strong driving force for assembly of strongly-welded, porous supraparticles under vacuum conditions. Interaction forces are significantly larger than those found in earlier simulations of the aggregation of smaller nanoparticles, indicating that supraparticle assembly using large 30 nm nanoparticles may be kinetically controlled. The porosity programmed into kinetic assembly may potentially benefit emerging applications of nanoparticle assemblies in medicine, in particular the development of nanostructured drug-eluting stent coatings. Future work will involve potential of mean force calculations in a variety of solvents to estimate the porosity obtainable for specific applications.

Received 4th February 2013,
Accepted 8th April 2013

DOI: 10.1039/c3cp50523e

www.rsc.org/pccp

Introduction

The self-organization of organic-coated inorganic nanoparticles into two- and three-dimensional superlattices provides new mesoscopic materials for electronic devices^{1,2} given their demonstrated collective magnetic, optical, and charge transport properties.^{3–11} These materials provide a direct means of setting macroscopic physical properties by nano scale engineering.¹² Fine-tuning the driving forces underlying nanoparticle self-organization requires detailed multi-scale experiments and simulations (see for example ref. 13 and 14) and so the purpose

of the present work is to probe the mechanism of supraparticle assembly using integrated nano and meso scale computer simulations. The observed superlattices arise *via* individually weak non-covalent interactions between the chemical coats on each nanoparticle^{15–19} that, summed over many interacting nanoparticles, provide tightly-woven and extensive self-assembled structures. Hence small nanoparticles, on the order of 1–10 nm in diameter, exhibit thermodynamically controlled assembly into ordered, self-correcting arrays.^{13,14} A parallel strand of research in nanoparticle organization is the use of linker molecules to covalently bind the (again, generally sub-10 nm) particles.²⁰ Although providing direct molecular tunnel junctions between the nanoparticles,²⁰ the strong chemical bonding can hamper self-healing of the assemblies.

In the present work, molecular simulations describe the structure, dynamics and energetics of nanoparticles aggregating *via* physical contacting of their hydrophobic molecular coats^{21–23} and nanoparticle deposition on bare and coated surfaces.^{24–26} We focus on the non-covalent self-assembly of large, alkyl-coated 30 nm-diameter nanoparticles. Such large nanoparticles are much less studied than smaller, typically sub-10 nm, particles and their

^a Theory, Modelling and Design Centre, Tyndall National Institute, University College Cork, Cork, Ireland. E-mail: damien.thompson@tyndall.ie; Tel: +353 214904063

^b Institute of Physics, Polish Academy of Sciences, Al. Lotnikow 32/46, 02-668 Warsaw, Poland

^c Institute of Theoretical Physics, Faculty of Physics, University of Warsaw, ul Hoza 69, 00-681 Warsaw, Poland

† Electronic supplementary information (ESI) available: Detailed computational methods, control simulations, extraction of supraparticle roughnesses and sedimentation profiles. See DOI: 10.1039/c3cp50523e

~30 nm diameter means their aggregation may differ from the fluid-like, self-healing arrays assembled using smaller nanoparticles¹³ and the rigid arrays formed by chemically fusing the nanoparticles.²⁰ The simulations in the present work indicate that the assembly may exhibit useful features of both, combining self-healing at the molecular scale with the formation of stable (rigid, long-range ordered) superlattices. These features are made possible by the large number of alkyl chain-chain interactions at each nanoparticle-nanoparticle interface, which provides a large driving force for aggregation. The computed atomic scale interaction potentials are mapped to a coarse grained potential that shows micron scale aggregation into kinetically stable, porous supraparticles under vacuum conditions.

In effect, the deep interaction wells coupled with the short range of the interactions between alkyl chains relative to the large size of the 30 nm particles hinders assembly of the thermodynamically most stable supraparticle that would have all buried nanoparticles in high coordination sites; we find instead kinetic trapping of individual nanoparticles at their “landing” sites on the growing multi-nanoparticle cluster, which gives porous supraparticles. Future work will involve potential of mean force calculations in a variety of solvents to quantify the effects of solvent steric hindrance and dielectric shielding on the strength of the potentials.^{17,26,27}

A number of recent simulation and experimental findings motivate the multi-scale modelling approach presented in the current work.

(1) Brownian dynamics simulations can identify mesoscopic assembly mechanisms that help explain experiments,¹⁴ hence we use interaction potentials computed at the atomic scale to parameterise a more coarse grained potential energy function that describes meso scale formation of many-particle clusters.

(2) Although the alkyl coats on small sub-10 nm nanoparticles are known to interact strongly through van der Waals forces, with aggregation strength increasing with both nanoparticle size and chain length,^{27,28} the interactions of larger nanoparticles are much less studied.^{29,30} Hence we investigate the aggregation mechanism and binding forces between large 30 nm nanoparticles coated with hexadecanethiol (C16) molecules.

(3) Alkyl-coated nanoparticles do not aggregate well in “good” (in this case, non-polar) solvents,^{27,28} hence to be able to form the particle-particle interfaces in reasonable computational time, we performed the atomistic simulations in vacuum. This provides an upper limit of aggregation strength; future work will model solution-phase aggregation in different solvents.

(4) Equilibrium, non-steered simulations require long sampling times,²⁵ hence we perform 10 ns nano scale dynamics for each complex, summing to 0.4 μ s overall; the structures and interaction energy estimates generated in the present work will provide starting structures and forces for future potential of mean force simulations.^{31,32}

(5) Heating lowers the effective attraction potential without changing the interaction distance,²⁷ hence we performed nano

scale simulations at room temperature and meso scale simulations at an effective temperature parameterised from the nano scale simulations. We also performed control simulations at elevated temperatures and observed more fluid-like assemblies.

(6) Semi-coarse grained, in particular “united atom”, models provide a molecule-level model of alkyl chain interactions.^{15,27,28,33} Given the need to quantify atomic level interaction strengths for the less-studied, large 30 nm-diameter nanoparticles, we used a more detailed, all-atom model for the nano scale simulations.

(7) Periodic models can introduce artificial ordering of supraparticles,²⁸ hence we used large simulation cell sizes for Brownian dynamics that permit unconstrained aggregation.

Motivated by these and other recent studies discussed below, we focus on large, 30 nm nanoparticles and start from the most physically sound all-atom model to estimate the interaction strength between their chemical coats. We then use the calculated interaction potentials to model, using more coarse grained Brownian dynamics, the formation of supraparticles *via* multi-particle aggregation. We find that the 30 nm nanoparticles form very tightly coupled interfaces under vacuum conditions, which leads to kinetic trapping of individual nanoparticles and which may provide routes to synthesis of porous supraparticles, though practical applications will require careful selection of solvent and ionic strength to tune the particle-particle interaction.

Methods

Atomistic molecular dynamics simulations

59 400-atom models were used to describe the alkanethiol-coated gold surface, with 900 hexadecanethiol chains arranged in a $2\sqrt{3} \times 3$ self-assembled monolayer (SAM) unit cell³⁴ to give a packing density of 4.5 molecules per nm². The chains adopt a tilt angle of 30°^{35,36} on a five-layer, 13 500-atom Au(111) square cuboid with surface dimensions *a* and *b* of 14 nm. The 30 nm-diameter nanoparticle surface curvature was modeled by defining a series of spheres of radius 1, 2 and 3 nm around the central gold atom and then shifting down 1, 2 and 3 gold layers to make the 30 nm nanoparticle surface, as shown in Fig. 1a, with the three selections illustrated using the blue, red and grey triangles. The nanoparticle surface was then coated with hexadecanethiol (Fig. 1b) molecules, as shown in the inset of Fig. 1a. Selection of alternative sphere radii would allow for a wide range of particle curvatures (radii) to be modelled in the future using this simple protocol (as we expect particle curvature to have a large effect on the aggregation strengths, from the data presented here for 30 nm particles and literature data on smaller nanoparticles).

The coated surface and nanoparticle models were combined in large simulation cells to extract interaction potentials. The distance between pairs of non-bonded atoms for inclusion in the pair list was set to 13.5 Å with a 12 Å cutoff and a switching function used between 10 and 12 Å. The atomic scale simulations required four model types and thirty-five model variants in all: fourteen to describe (1) the interaction between coated

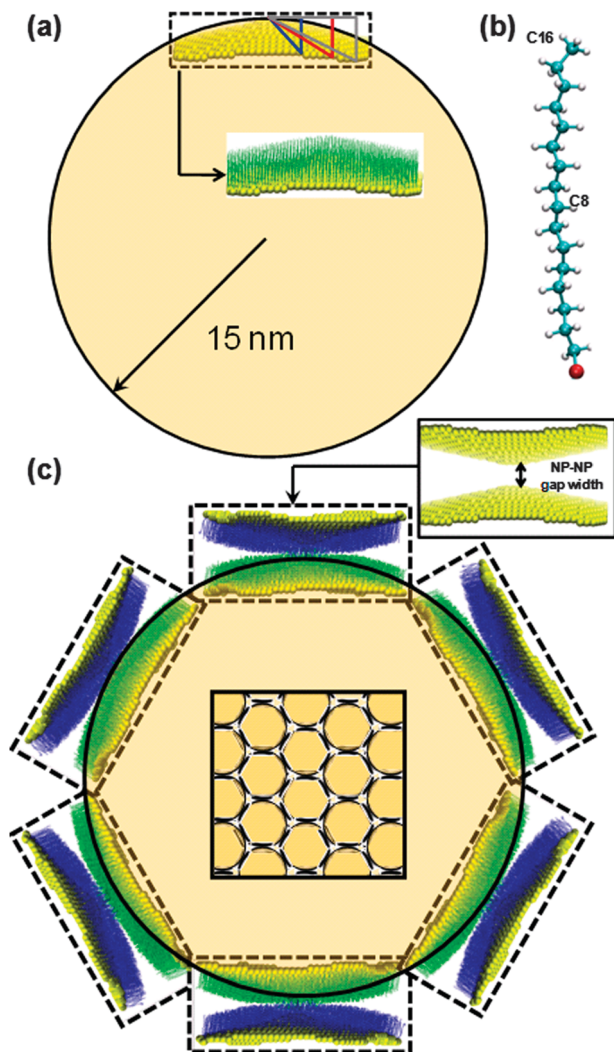


Fig. 1 (a) Projection of the curved, hexadecanethiol-coated Au(111) surface model (inset) onto the surface of a 30 nm-diameter nanoparticle. The hexadecanethiol molecules are shown as green lines with hydrogen atoms omitted for clarity. (b) One hexadecanethiol molecule, shown in ball-and-stick representation with light-blue, white and red spheres for the carbon, hydrogen and sulfur atoms. The sulfur atom bonds the molecule to gold while the terminal methyl CH_3 group at the other end of the alkyl chain is exposed at the surface of the coated nanoparticle. (c) 2-D projection of the coated 30 nm nanoparticle, from the calculated most stable interface structure given in Fig. 2(a), with the inset at the top righthand corner showing the vertical gap separation between nanoparticles. The inset panel shown inside the nanoparticle sphere sketches a horizontal 2-D projection of the resulting hexagonal crystal packing of 30 nm nanoparticles to form an ordered superlattice.

flat surfaces; seven for (2) the interaction between coated 30 nm nanoparticles; eight for (3) the interaction between a coated flat surface and a bare flat surface; and finally, six to describe (4) the interaction between a coated 30 nm nanoparticle and a coated flat surface. The crystallographic (as opposed to continuous) model used to generate a first approximation to the atomic scale particle surface structure is appropriate for room temperature studies.¹⁵ Other surface topographies are possible apart from the one we choose to model in the present study (Fig. 1a); the large surface area of the 30 nm nanoparticles

means we may expect a large variety of near-isoenergetic shapes and surface geometries. The NAMD program,³⁷ together with the CHARMM22 force field,³⁸ was used for room temperature Langevin molecular dynamics with a NVT ensemble (constant number of particles, constant volume and constant temperature). Gold atoms were constrained to their starting crystallographic positions throughout the simulations and given standard CHARMM22 van der Waals potentials,³⁸ and a 2 fs timestep was used for dynamics by constraining covalent bonds to hydrogen using the ShakeH algorithm.³⁹ Each model was relaxed using 2000 steps of steepest descent minimization and then brought to room temperature by gradually raising the temperature from 0 to 295 K over 2 nanoseconds of dynamics while simultaneously loosening positional constraints on the alkanethiol heavy atoms. The final 2 ns of each 10 ns production run were used to generate energy vs. distance interaction profiles, sampling every 20 ps over 100 statistically-independent structures and extracting the nanoparticle–nanoparticle and nanoparticle–surface interaction energies, summed over van der Waals and electrostatic interactions. Image generation and Tcl script-based trajectory analysis were performed using the VMD program.⁴⁰ Further computational details are provided in ESI,[†] Section S1.1.

Meso scale molecular dynamics simulations

To model meso scale multi-nanoparticle aggregation, we extracted effective coarse grained interaction potentials from the atomistic data. We use the potentials derived for the specific case of long chain alkanethiol molecules on gold nanoparticles under vacuum conditions, which neglects solvent interactions and electronic interactions between the gold cores, and serves as a model for more general hydrophobic molecule-mediated assembly of supraparticles, including for example, networks of lauric acid-functionalized cobalt nanoparticles.^{3,4,7,9–11}

The atomic scale potentials describe the thermodynamics of individual interfaces A–B. For example, the interface between two nanoparticles A and B or the interface between nanoparticle A and surface B. We use these computed potentials to extrapolate to collective mesoscale behaviour using coarse grained simulations that contain these A–B sticking potentials. The mesoscale simulations illustrate the types of architectures that arise under conditions of assembly in the absence of hindrance from solvent molecules, *i.e.*, the strongest interaction theoretically obtainable between A and B. We find that the rapid, simultaneous formation of multiple, strong interfaces leads to the formation of porous assemblies in which individual nanoparticles may be trapped in low-coordination sites in the supraparticle matrix.

The meso scale models simulate the formation of supraparticles by nanoparticle aggregation in bulk and near attractive/repulsive surfaces. We consider N nanoparticles (the maximum number used is $N = 5954$) in a cubic box with size l up to 1.5 μm . There are periodic boundary conditions in the planar x and y directions. The evolution of the system is then studied using Brownian dynamics⁴¹ simulations.

The atomic scale potentials given in Results indicate that the interaction energy becomes significant at separations below

around 4.5 nm. To describe the interactions between nanoparticles we fit the potential to a standard 6–12 Lennard-Jones potential with well depth and position set according to Fig. 2a in Results. This corresponds to -16.2 eV for 900×2 hexadecanethiol chains on two large 30 nm particles (*i.e.*, 1800×-0.009 eV per chain) at $s = 2.3$ nm separation. For interaction with an attractive wall, the potential well corresponds to -72 eV (from Fig. 4a in Results, for 900 chains on a large 30 nm particle and 900 chains on a coated surface, *i.e.*, 1800×-0.040 eV per chain) and the minimum is at $s = 2.8$ nm separation. Note that the interaction of a coated surface with a bare gold surface (described in Section S2.2 of ESI†) gives a similarly large value for particle–surface interaction, -63 eV, from 900×-0.070 eV per chain. We represent the 30 nm particle interaction with the coated surface by the 3–9 potential as given by

$$V_{(\text{NP-wall})} = \frac{3\sqrt{3}}{3} \epsilon_{\text{NP-wall}} \left[\left(\frac{\sigma_{\text{NP-wall}}}{s_{\text{NP-wall}}} \right)^9 - \lambda \left(\frac{\sigma_{\text{NP-wall}}}{s_{\text{NP-wall}}} \right)^3 \right] \quad (1)$$

where the parameter λ allows for switching between the attractive ($\lambda = 1$) and repulsive walls ($\lambda = 0$). The parameter $\sigma_{\text{NP-wall}}$ is derived from the location of the minimum when $\lambda = 1$. Both the nanoparticle–nanoparticle (NP–NP) and NP–wall potentials are cut at $s = s_c$, with s_c estimated as $s = 4.5$ nm from Fig. 4b in Results, over twice the length of two extended hexadecanethiol molecules (2×2.0 nm). For the surface interaction the top wall is the same as the bottom wall and the particles are initially placed uniformly within the volume with the condition that the gap separation (from both the top and bottom walls) is at least twice the NP radius.

Wang *et al.*⁴² recently described model potentials for the interaction between gold nanoparticles, including Morse, Lennard Jones and Hamaker potentials, and derived a correction to account for the interaction between the alkyl molecule coats. The resulting potential showed a deep attraction energy well,⁴² of similar shape to those derived from the atomistic molecular dynamics simulations in the present work, and the general approach⁴² proved useful for mapping the range of parameter potentials governing self-assembly. Although the “united atom” or semi-coarse grained MARTINI model used in ref. 28 captures aggregation in great detail, the nanoparticles are very small, ~ 1 nm, and the aggregation is limited to just 8 nanoparticles per cell. By contrast, we model cells containing up to several thousand 30 nm nanoparticles. In common with ref. 28 we use Brownian dynamics, and we direct the simulations towards long timescales by using gravity to speed up aggregation. Finally, very recent simulations¹³ have modelled the self-organisation of polydisperse nanoparticles into remarkably well-ordered supraparticles using a complex model that includes long-range Lennard-Jones forces as well as electrostatic repulsion that depends on both the size and position of the nanoparticles, with a different dielectric constant used for buried sites inside the supraparticle and free solvent. The effective reduced temperature T^* used was between 0.2 and 0.7 for the ~ 3 nm-diameter nanoparticles.¹³ The very steep and deep cohesive energy profile we calculate in the present work

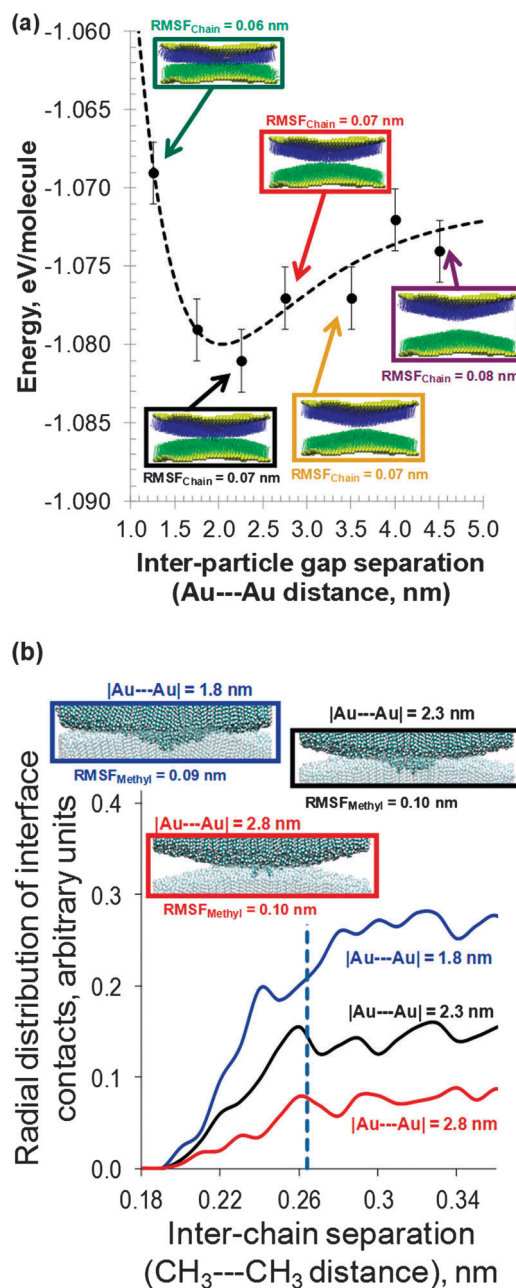


Fig. 2 (a) Interaction profile for 30 nm hexadecanethiol-coated nanoparticles, showing interaction energies (eV per molecule) vs. gap width (nm). Error bars on each point show the standard deviation over 100 molecular dynamics structures (sampling every 20 ps over the final 2 ns of 100 ns room temperature dynamics). The functional form of the Morse potential fit to the data in this plot and the forms of the fits in all subsequent plots of energy vs. separation are given in Table S1 (ESI†). Representative molecular dynamics structures, together with time-averaged root mean square fluctuations (RMSF) for molecules are given in the inset panels; Au atoms are shown as van der Waals's spheres and alkanethiol chains are shown as sticks, coloured blue and green to distinguish between chains on each face, with hydrogen atoms omitted for clarity. (b) Radial distribution functions (RDF) for contacts between terminal methyl groups on opposing particles. In this case the molecular dynamics structures show the chain structure at the interface, with carbon and hydrogen atoms shown as light blue and white spheres and one monolayer made partially transparent to distinguish between layers. The blue, black and red curves show RDFs for interfaces constructed from 1.8, 2.3 and 2.8 nm gap separations as marked in panel (a), and the dashed vertical line marks the target 0.264 nm H...H separation³⁸ at the interface.

for the interaction of 30 nm particles, corresponds to a much lower T^* on the order of $kT/\varepsilon = 0.001$, where ε is a characteristic depth of the energy well; more details are in ESI†, Sections S1.2 and S2.3.

Results

We first describe the atomic resolution molecular dynamics simulations of room temperature nanoparticle–nanoparticle and nanoparticle–surface interactions and then present the more coarse grained mesoscopic simulations of many-nanoparticle aggregation and surface deposition.

Molecular dynamics of the interface between 30 nm-diameter nanoparticles

Fig. 2a shows the computed interaction potential for 30 nm-diameter nanoparticles. Interaction energies are the sum of the van der Waals and electrostatic energies of the chain–chain interactions in the complexes, expressed as energies per chain, for ease of comparison of the current dataset with literature values for different nanoparticle types, sizes and chain coverages. The corresponding molecular structures show that the curvature of the particles allows for close contacting of the molecular coats on opposing particles, reducing the separation to just 2.3 nm at the closest point of contact. Although the chain coats on the 30 nm-diameter nanoparticles adopt ordered SAM conformations as opposed to the splayed or dome-like²⁸ structures found for smaller particles, the degree of cohesion remains significant. The 2.3 nm gap width between particles is sketched in the inset of Fig. 1c and is just over $\frac{1}{2}$ the separation calculated in control simulations of flat surfaces described in ESI† (S2.1), highlighting the dramatic reduction in inter-particle gap width due to increased attraction between curved surfaces.⁴³

The well depth for individual chain–chain interactions (*i.e.*, the interaction force per alkanethiol molecule) in Fig. 2a is relatively shallow, with the time-averaged uncertainty in the chain energies a significant proportion of the difference in energies between datapoints. Such a shallow per-chain potential may be expected for the low surface curvature of the 30 nm-diameter particles compared to smaller particles with diameters in the range 1–10 nm.^{14,27} Smaller diameter nanoparticles have more curved surfaces, allowing more significant interdigitation of chains at the particle–particle interface. The potential in Fig. 2a plateaus for separations ≥ 4.0 nm to a baseline energy of $-1.07(3)$ eV per chain, corresponding to dissociated particles with $\sim 85\%$ of the -1.24 eV chain stability in the monolayer films on reference flat surfaces (Fig. S1a, ESI†). The curvature of the 30 nm particle provides a soft potential for chain–chain interactions, with penalties of ≤ 0.01 eV nm⁻¹, Fig. 2a for all but the step from 1.8 nm \rightarrow 1.3 nm gap width (horizontal axis of Fig. 2a). This final contraction of the inter-particle gap to just 1.3 nm is as expected very unfavourable, with cramped chains giving repulsion penalties of $+0.02$ eV nm⁻¹. Nevertheless, the repulsion penalties are ~ 6 times smaller than those obtained for the

interaction between reference flat surfaces (Fig. S1a, ESI†), as significant chain entanglement occurs between nanoparticle faces even with nanoparticles as large as 30 nm.

The radial distribution function (RDF) plots in Fig. 2b map out the interactions between terminal methyl groups on opposing particles. The plots show that the computed optimum separation of 2.3 nm (black curve) gives a large population of nearest neighbour contacts centered around the most favourable H \cdots H separation of 2.64 Å.³⁸ By contrast, the 0.5 nm closer separation to 1.8 nm (blue curve) gives a large population of repulsive hydrogen overlaps. Although there are more 2.64 Å contacts at the 1.8 nm separation, the presence of a high population of additional repulsive hydrogen contacts make the 2.3 nm gap separation more energetically favourable. The 0.5 nm further separation to 2.8 nm (red curve) is also unfavourable as this extra separation reduces the population of favourable van der Waals contacts. Root mean square fluctuation (RMSF) values in Fig. 2a show that, at the largest separation of 4.5 nm, the chain flexibilities for the 30 nm nanoparticle are only slightly larger than for the reference flat surface, 0.08 nm *vs.* 0.06 nm (Fig. S1, ESI†).

Fig. 3a shows the conformational space sampled by representative chains over the final 2 ns of dynamics for the closest 1.3 nm, optimum 2.3 nm and dissociated 4.5 nm separations in Fig. 2a, illustrating how increasing the inter-particle separation makes the chains become slightly more flexible. As their conformational freedom increases, the molecules vibrate with increasing amplitude around a mean position, as RMSF values increase from 0.6 to 0.8 Å. Fig. 3b highlights the position of the terminal methyl carbons on one of the particles in the final structures generated following 10 ns of dynamics. The structures show the transition from, at the most unfavourable 1.3 nm separation (Fig. 2a), a large central defect region surrounded by an ordered periphery (Fig. 3b), through to the smaller defect central patch surrounded by the large area of highly ordered chains at the optimum separation of 2.3 nm, and finally the most ordered arrangement on the surface of the dissociated particle at 4.5 nm inter-particle gap separation. Fig. 3c overlays the terminal carbons of the second particle, which are coloured from red to white to blue in each structure as the distance between the particles increases. This overlay shows how a small amount of interdigitation at the centre of the particle–particle interface enhances the overall three-dimensional ordering in the complexes. Although the chain dihedral angles and tilt angles in Fig. 3b show that the alkanethiol coats on the 30 nm particles form SAMs very similar to those on flat Au(111) substrates, Fig. 3c shows the major difference due to curvature. The vertical chain interdigitation (over a small portion of the overall particle surface area, as sketched in Fig. 1) stabilises the optimum 2.3 nm separation, with the inset panel in the center of Fig. 3c showing a zoom-in on the interdigitated chain structure that stabilises the optimum 2.3 nm separation. As shown in the inset plot of gauche defect populations in Fig. 3b, the population of bent chains⁴⁴ decreases significantly as the inter-particle gap width is relaxed from 1.3 nm to 2.3 nm, giving more ordered monolayers.

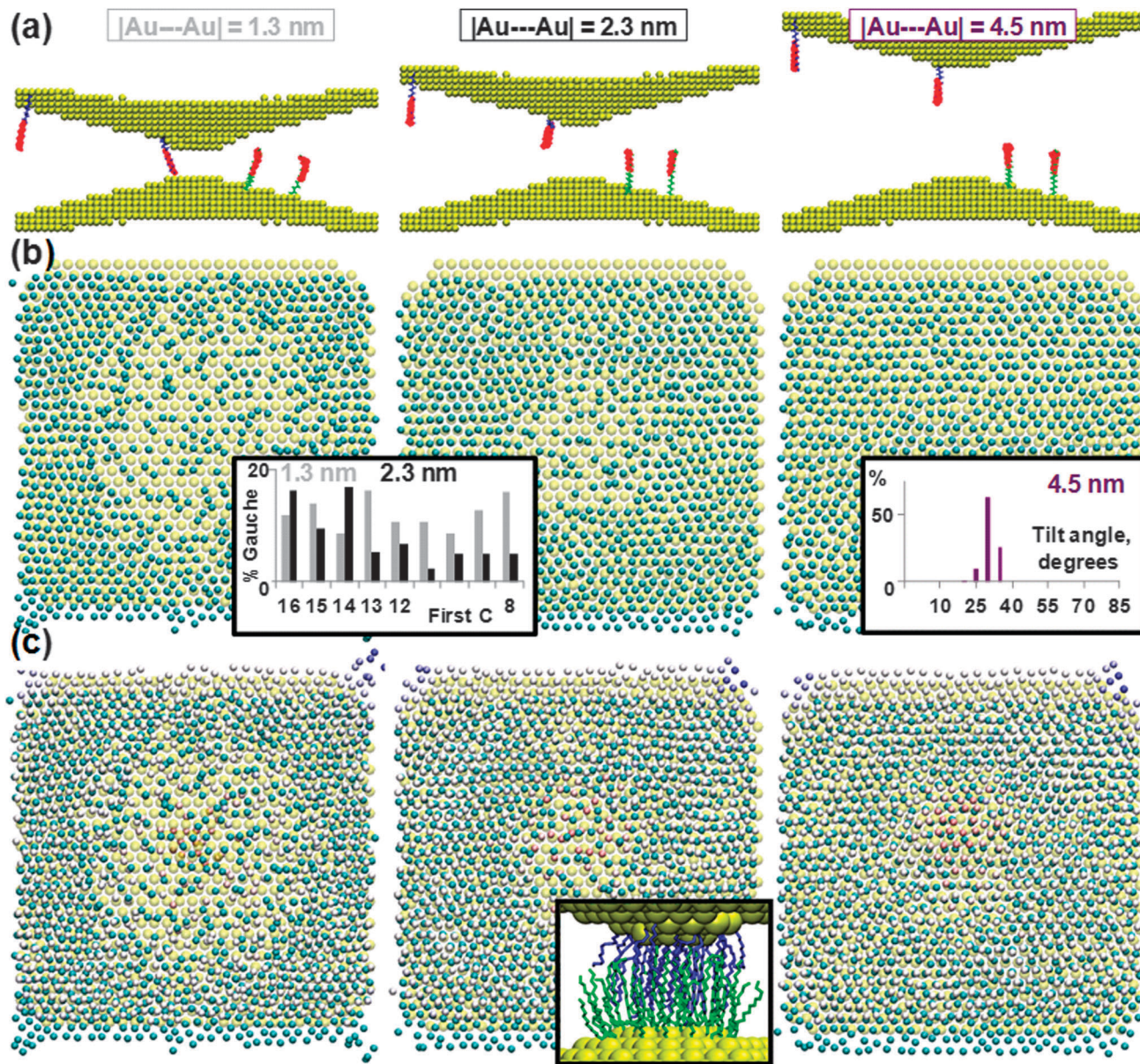


Fig. 3 (a) Carbon atom time histories for selected molecule chains at the closest 1.3 nm, optimum 2.3 nm and furthest 4.5 nm inter-particle gap separations, for 100 equally-spaced structures over the final 2 ns of dynamics. (b) Terminal methyl packing in the corresponding molecular dynamics structures, with the second nanoparticle removed for clarity. Inset panels are described in the text and show (left) computed chain gauche defect populations for the 1.3 and 2.3 nm separations, and (right) chain tilt angles for the 4.5 nm separation. (c) Inter-particle methyl packing, with carbon atoms in the second particle coloured red to white to blue radiating outwards from the center. The inset of the middle panel shows a zoom-in on the central interdigitated chain structure that helps stabilise the optimum 2.3 nm particle–particle gap width.

“First C” for the gauche populations is carbon number n in the $(n, n - 1, n - 2, n - 3)$ chain segment that defines the measured dihedral angle. The total percent of gauche defects over the terminal 8 carbons, *i.e.*, from the terminal methyl carbon, C16, down to mid-chain C8 (Fig. 1b), is reduced from 12% to 8% on relieving bad contacts (Fig. 2b), with the defect population at the 4.5 nm separation decreasing to 1%, the same as that calculated for SAMs on flat Au(111).^{36,45} The inset distribution of chain tilt angles at the 4.5 nm separation show a value of $31^\circ \pm 4^\circ$, indicating that SAMs on the non-contacted 30 nm particles adopt $\sim 30^\circ$ angles similar to SAMs on Au(111),^{34,36,45}

in agreement with the computed decrease of tilt angles to near- 30° as nanoparticle size is increased.¹⁵

Molecular dynamics of nanoparticle–surface interactions

A second set of atomistic molecular dynamics simulations measured the interaction between a 30 nm nanoparticle and an alkanethiol-coated flat gold surface. Fig. 4a shows the computed interaction potential, with the most stable time-averaged chain energy of $-1.14(3)$ eV occurring at a separation of 2.8 nm. The corresponding molecular structures show that optimised van der Waals contacts promote the formation of the

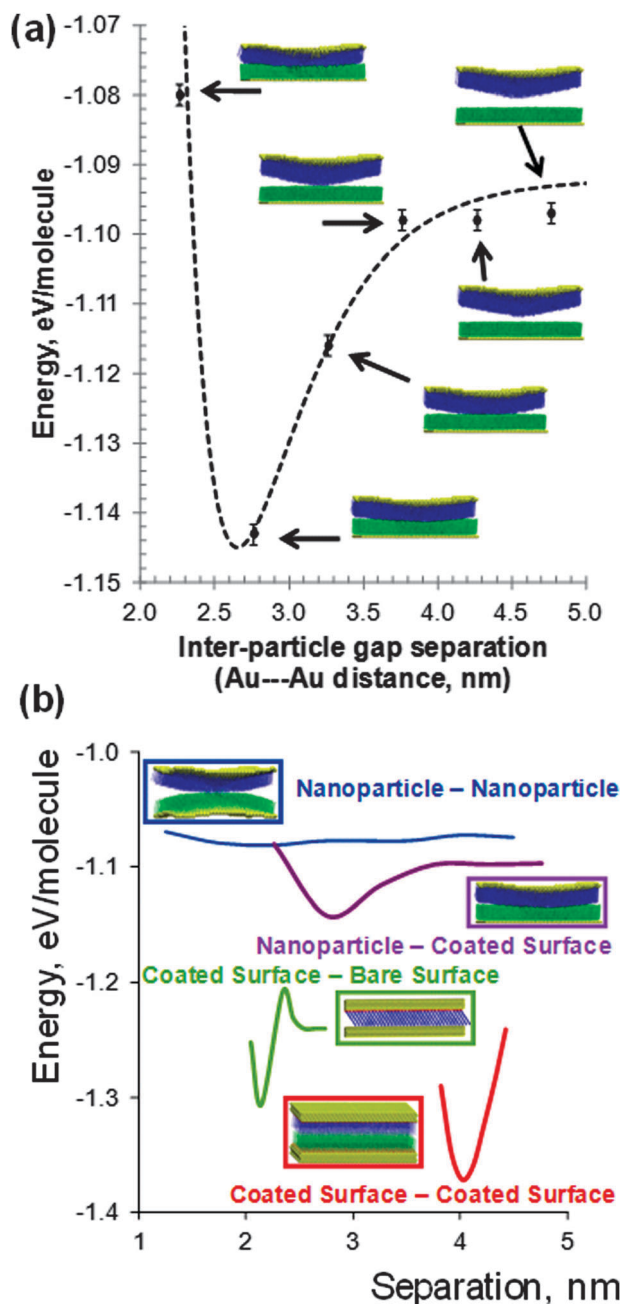


Fig. 4 (a) Interaction profile for a 30 nm coated nanoparticle interacting with a coated surface. See Fig. 2 legend for more details. (b) All interaction potential data plotted together; coated surface-coated surface (Fig. S1a, ESI[†]), nanoparticle-nanoparticle (Fig. 2a), coated surface-bare surface (Fig. S3a, ESI[†]) and nanoparticle-coated surface (Fig. 4a). The interface structures that give these different strength potentials are sketched in ESI[†] Fig. S4 and discussed in more detail on pages S10–15.

complex at 2.8 nm, intermediate between the large gap separation of 4.0 nm for two flat surfaces (Fig. S1a, ESI[†]) and 2.3 nm found for the interaction between the 30 nm particles (Fig. 2a).

For ease of comparison, all the interaction potential data are plotted simultaneously in Fig. 4b (including also the two reference systems described in ESI[†] Section S2). The interaction potential for the 30 nm particle with the coated surface

is much sharper, and deeper,⁴³ than that obtained for the 30 nm particles in Fig. 2a, due to the larger number of contacts formed with the SAM on flat Au(111).

The penalty of 0.12 eV nm^{-1} in chain-chain interactions for shifting to the smaller gap of 2.3 nm reflects the cost of breaking the chain packing on the coated surface. This repulsion penalty, though significant, is approximately $\frac{1}{2}$ the 0.22 eV nm^{-1} penalty when both surfaces are flat (comparing the purple and red curves in Fig. 4b; see also Fig. S1a and S4, ESI[†]), reflecting the greater conformational freedom of the molecules when bound to the 30 nm particle surface, which allows for formation of the closer particle-surface contact (purple curve in Fig. 4b).

Finally, the particle-particle (blue curve in Fig. 4b) and particle-coated surface (purple curve) potentials go to similar, but not equal, asymptotic values at large separations. This is due to the curvature, and hence less ordered SAMs, of the 30 nm surface.

Bulk and near-surface supraparticle assembly

We now present supraparticle structures calculated using the atom-parameterised mesoscopic model described in Methods. Briefly, to model many-nanoparticle aggregation into supraparticles, the atomistic potentials were mapped onto a more coarse grained, modified Lennard-Jones potential for particle-particle interactions.^{46,47} The coarse grained Brownian dynamics simulations confirm that very strongly bound assemblies are formed when alkanethiol-covered 30 nm nanoparticles aggregate under certain conditions, *e.g.*, in the presence of a solvent that does not significantly impede chain-chain interactions. The simulations show that the assembled supraparticles can form extended, porous assemblies on surfaces.

In the first instance, we probe deposition on a flat surface. The surface is a meso scale representation of the coated surface given in atomic detail in Fig. 4a, with a uniform coating of molecules, and we model the surface wetting by the 30 nm nanoparticles using the coarse grained model in which a sphere represents the nanoparticle and the solvent is implicit (details are in ESI[†] Section S1.2). In addition to the attractive wall, we also consider situations in which the interaction with the surface is repulsive.

Fig. 5 illustrates the difference between the structures obtained in the vicinity of the attractive and repulsive walls, from models containing 277 nanoparticles in a box of 500 nm edge length (see Methods for details). The first half of the surface ($x = 0-250 \text{ nm}$) is repulsive and the second half is attractive. Fig. 5a shows the arrangements of the particles in the horizontal x - y plane. The arrangements at the attractive and repulsive regions appear similar when viewed from above. However, there is a noticeable difference in the vertical arrangements (Fig. 5b). Above the attractive surface the gap separations are around $s_A = 2.8 \text{ nm}$ and their variations are sub-Angstrom, providing a (moderately dense) monolayer coverage. On the other hand, above the repulsive region, the particles hover at a higher elevation, at $s_R = 4.2 \text{ nm}$ and the standard deviation is 0.21 nm . The larger scatter above the repulsive region is due to the lack of a

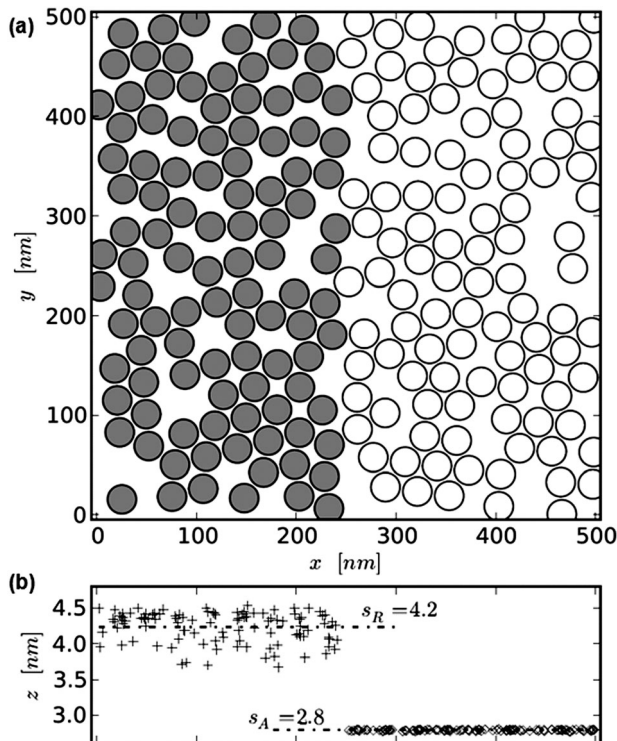


Fig. 5 (a) The monolayer of 277 nanoparticles deposited on a surface which is repulsive in one region ($x < 250$ nm) and attractive in another ($x > 250$ nm). The locations of the particles are shown in the horizontal x - y plane. The darker circles correspond to particles above the repulsive region. (b) The gap separation of the nanoparticles above the surface.

minimum in the repulsion potential (details are in ESI,[†] S1.2) and hence larger role of even tiny $k_B T$ thermal fluctuations.

When the aggregation of a larger number of particles is considered, multi-layer films are formed. Such layering is shown in Fig. 6a for 5954 nanoparticles aggregating at an attractive surface,

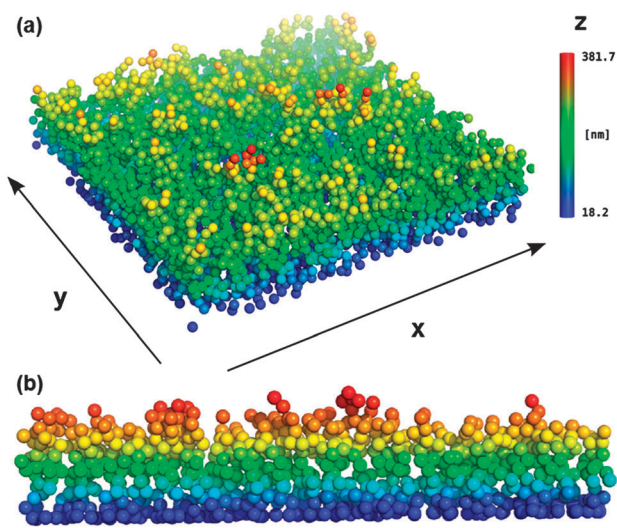


Fig. 6 (a) Effect of sedimentation of 5954 nanoparticles on the attractive surface in the box of length $l = 1500$ nm. The shades indicate the magnitude of the elevation. (b) A slice of width 210 nm of the system shown in panel (a).

with the cell length increased to 1.5 μm . A cross-section of width 210 nm (in the y -direction) is shown in Fig. 6b. Packing between nanoparticles remains loose even in these higher concentration systems, and so porous 3-D structures are formed. The volume fraction is about 0.23 when measured below the average elevation of the top surface of the film shown in Fig. 6b; the porosity is then about 0.77. The reason for the high porosity is that the particles get glued together on encounter due to the very high inter-particle binding strengths (summing the per-chain interaction strengths to estimate per-particle strengths is described in Discussion) and are hence frozen at their “landing” sites on the growing multi-nanoparticle cluster. In terms of Brownian dynamics, the corresponding low effective temperature regime offers very little sideways diffusion and no reorganisation. The supra-particle surface roughness is discussed in more detail in ESI,[†] Section S3.

In order to better understand the origin of the large porosity in the films, we consider a system that allows for a geometric control of the growth process. Specifically, we model an aggregation process in which the attractive wall hosts sedimentation from two localised sources. Each source emits nanoparticles downwards with the Gaussian density of width a within a horizontal plane. The centers of the two sources are separated by S . The sedimented structures obtained for $N = 500$ are shown in ESI,[†] Fig. S7. For large values of separation S the process results in formation of separate columns that are rough on the sides. The lateral roughness increases with column width a . When S decreases and/or a increases, the two columns begin to coalesce. The coalescence process is illustrated in Fig. 7, and shows that the columns grow together but again in irregular, kinetically trapped, geometries with a large void fraction. More fluid-like, partially healed assemblies are obtained at elevated temperatures (weakened interaction potentials) as shown in Fig. S5 (ESI[†]).

The coarse grained wall model we used above corresponds to a smooth surface. In experiments, the surface will have an atomic level corrugation and roughness that will introduce sideways static friction. This atomic level roughness is in

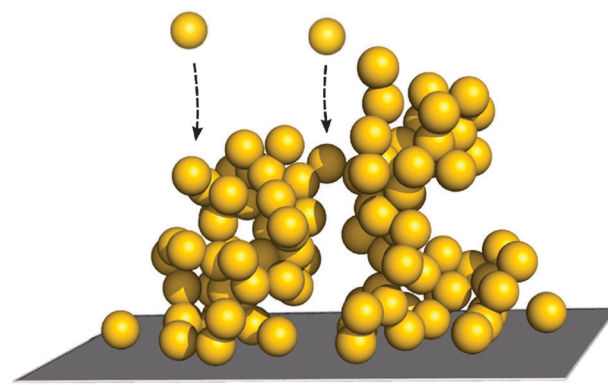


Fig. 7 A close-up view of an imminent coalescence of two separate columns of particles, for column separation of approximately 150 nm and column width of approximately 46.5 nm (Fig. S7, ESI[†]).

addition to micro/macro scale roughness, beyond the scope of the present simulations. In the case of the repulsive wall, the nanoparticles are further away (Fig. 5b) and thus less sensitive to the atomic scale topology, which can be modelled as lack of static friction. The repulsive wall can be realised experimentally by introducing a hydrophilic patch on the surface instead of the hydrophobic alkanethiol layer, for example, by replacing methyl terminal groups with alcohols.²⁸

Fig. 8 illustrates growth at a wall (that is shaped like a trapezoid along the x -direction), with two inclined planes, one repulsive and one attractive. The incline angle is chosen to be steep, at 68° . The first half of the wall (in the x direction, including the first half of the elevated top surface) is repulsive and the other half of the surface is attractive. The nanoparticles coalesce at the foot of the repulsive incline (top lefthand panel of Fig. 8). The attractive incline on the other hand, shown in the top right panel of Fig. 8, strongly binds the particles and initializes columnar growth similar to that described above. Interestingly, the presence of the steep “hill” between the attractive and repulsive regions results in the formation of overhanging structures at the top of the trapezoid, as emphasised in the bottom panel of Fig. 8. Such “overhangs” will contribute to the porosity of the supraparticle and may provide a means of forming large pores near the substrate, as well as at the top surface of the deposited structure. Although practical applications of nanostructures in medical devices require clever means of controlling phase transfer and bio-interactions,⁴⁸ one possible application of such porous surface coatings could be to encapsulate drugs and other active agents on the surface of stents and pacemakers for slow release in the body.

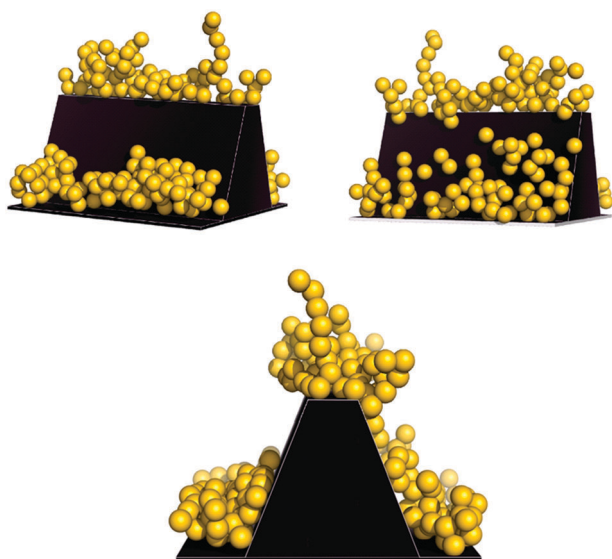


Fig. 8 A system with 242 nanoparticles in a box of length 500 nm. The height of the trapezoid is 250 nm, the top wall is 100 nm wide and the incline is at an angle of 68° . Half of the trapezoid surface is made repulsive, the other is made attractive. The top-left panel shows supraparticle growth on the repulsive incline. The attractive incline, shown in the top-right panel, leads to columnar growth akin to that shown in Fig. 7. The bottom panel presents a side view (along the x -axis) of the trapezoidal step, showing formation of an “overhang” in the structure.

Discussion

In this section the combined multi-scale simulation results are discussed in relation to the state of the art in self-organizing nanocrystal design and synthesis for electronics^{3–11} and health.^{48,49}

Estimated upper limits on the interaction forces between 30 nm-diameter particles

The higher position of the potential well minimum, -1.08 eV per chain for the 30 nm particles in Fig. 2b vs. -1.37 eV per chain for the reference flat surfaces in Fig. S1b (ESI[†]), originates from the contact geometries between molecular coats on opposing particles. Contacts between the 30 nm particles involve a small area of interdigitated chains near the center of the particle–particle interaction region and then gradually weakening van der Waals contacts between more distant chains (radiating outwards from the centre of the particle–particle closest contact), as shown in the molecular structures in Fig. 2 and 3 and sketched in Fig. S4 (ESI[†]). This “zoning” in the complexes dictates the interaction strength, and involves a balance between the strongly bound central zone and the more dissociated peripheral regions. The interaction potential between individual chains on associating particles is thus very weak for the pair of 30 nm particles with only a small preference for particular inter-particle gap separations within the range of approximately 1.8 nm to 3.5 nm. The time-averaged well depth (Fig. 2a) of approximately 9 meV per chain for optimum (2.3 nm) vs. dissociated (4.0 nm) separations in the pair interaction potential corresponds to average chain energies below room temperature thermal energies $k_B T \sim 26$ meV where k_B is Boltzmann’s constant and T is the absolute temperature. However, summing over the 900 chains on each nanoparticle segment (Fig. 1) gives a significant time-averaged benefit of ~ 8 eV per particle for pairing.

The potential may be considered additive within the limit of the accessible surface area of the particles and so formation of particle–particle interfaces will drive the assembly of supraparticles. In a 3-D hexagonally packed nanoparticle array (stacking the 2-D array sketched in the inset panel of Fig. 1c) each buried 12-coordinated particle can thus obtain huge particle stabilisation energies of ~ 97 eV per particle. This estimate then provides an upper bound of the maximum obtainable cohesive force available for packing large 30 nm-diameter particles; in solution-phase experiments solvent molecules will buffer the aggregation of the alkanethiol-coated particles.²⁷ The interdigitated chains in the inset panel in the center of Fig. 3c have inter-particle chain binding energies at least 10 times larger than those of the more distant chains, confirming that local intertwining of chains on opposing nanoparticle faces can drive aggregation in the presence of a solvent that does not significantly impede chain–chain interactions.

The most shallow well depth from Fig. 2a corresponds to the difference between the upper bound for the energy at 2.3 nm and the lower bound for the energy at 4.5 nm, -3 meV per chain. This well depth gives a lower limit for the packing energy of ~ 32 eV per particle in a buried 12-coordinated site in the

hexagonally-packed array of nanoparticles ($-0.003 \times 900 \times 12$), equivalent to the summed binding energy of eighteen -1.7 eV Au–S chemical bonds.⁵⁰ The net stabilisation remains significant for nanoparticles with sub-12 coordination numbers, with -2.7 eV (-0.003×900) obtained per coordinating nanoparticle. This large stabilisation obtained from alkyl chain contacting is exploited experimentally as an ordering element for the self-assembly of large-area multi-particle networks,^{3,4,51–61} as yet using generally smaller-sized sub-10 nm particles. Finally, for the corresponding 2-D gold particle arrays that provide long-range charge conduits for nanoelectronics,²⁰ the driving force for physical aggregation of alkyl-coated 30 nm particles (as yet untested experimentally) will remain strong. We predict that, under ideal conditions with minimal solvent buffering, the packing energy (prior to ligand exchange and covalent interlinking²⁰) will be at least 16 eV per particle for arrays of 6-coordinated particles (sketched in the 2D projection in Fig. 1c).

Qualitative comparison with computed interaction forces and aggregation mechanisms found for smaller nanoparticles

The computed interaction potential shapes and well depths (Fig. 4b) are qualitatively consistent with earlier studies of smaller coated particles^{14,27,33} as well as coated flat surfaces,³³ some of which were performed using different methods including potential of mean force calculations in the presence of solvent. Converting the interaction potential calculated for the 30 nm particles into units of $k_B T$ gives an extremely steep potential well depth on the order of $-620k_B T$ for pairwise interactions, with previous models giving values of approximately $-120k_B T$ and $-180k_B T$ for much smaller 1.8 nm and 2.7 nm particles coated with 58 and 136 dodecanethiol molecules respectively, with interaction seen to increase with both particle size and chain length.²⁷ Extrapolating well depths for hexadecanethiol-coated (Fig. 1b) particles from the chain length dependences given in ref. 27 gives estimated values of $-170k_B T$ and $-240k_B T$ for the 1.8 nm and 2.7 nm particles. Then using a log fit for the dependence of the interaction strength on surface chain coverage, we may estimate a well depth of $-410k_B T$ for the present hexadecanethiol-coated 30 nm particles using the data in ref. 27. Although this method of extrapolation is extremely basic and may not be expected to yield reliable quantitative measures of radii-dependent interaction forces, the estimate of $-410k_B T$ indicates a very strong interaction. We note that this estimated value is qualitatively similar to (approximately two-thirds as large as) the time-averaged value of $-620k_B T$ we calculate directly from the present simulations. The extrapolated value of $-410k_B T$ falls within the large time-averaged uncertainty in our data (with a minimum interaction potential of $-210k_B T$ estimated from the error bars in Fig. 2a). More generally, the same trends of steeper repulsion penalties for larger particles, deeper attraction wells and narrower-shaped potentials (Fig. 4b) were seen in the previous study of small sub-5 nm particles.²⁷

Overall then, we can propose that aggregation of large 30 nm-diameter nanoparticles involves very large inter-particle cohesive forces due to the large number of chains at each

particle–particle interface. The very strongly welded multi-particle clusters found in the atom-parameterised Brownian dynamics simulations support this hypothesis. On the other hand, the more shallow interaction potential for smaller nanoparticles^{14,27} allows for assemblies that can self-heal not only at the atomic scale of chain–chain interactions but also at the scale of the full particle–particle interaction. This particle-level correction is not available for the 30 nm particles under room temperature vacuum conditions, as discussed in more detail on pages S10–15. Although the atomic scale chain–chain interactions remain fluid, the 30 nm nanoparticle position is trapped at its “landing site” on the supraparticle due to the very large cumulative cohesive force between the particle faces.

A very recent combined experiment–simulation study¹³ showed formation of surprisingly low-polydispersity supraparticle spheres from the assembly of ~ 3 nm nanoparticles, that may be intermediate between smaller particles that give fluid-type, less ordered assemblies and larger particles (such as the 30 nm particles modelled in the present study) that give “welded” aggregates. Such welded supraparticles may be kinetically trapped in irregular geometries, with the very strongly coupled particle–particle interfaces preventing the rolling of individual particles to more stable sites and so blocking access to the most thermodynamically stable configurations that would produce more densely packed, more regularly shaped assemblies. The different assembly regimes are sketched in Fig. S4 (ESI†) and control Brownian dynamics simulations (Fig. S5, ESI†) indicate that a more fluid-like assembly is obtained for the large 30 nm nanoparticles at higher temperatures (weaker interaction strengths).

Conclusions

The present study provides further details on the atomic scale mechanism underlying the physical aggregation of inorganic nanoparticles coated with hydrophobic alkyl films, and the derived interaction potentials are mapped onto a more coarse grained potential to describe the meso scale self-organisation of the coated nanoparticles into supraparticles. The computer model confirms and extends the major features observed in the earlier studies. The energy minimisation achieved by optimising inter-chain contacts between coated nanoparticles drives the two- and three-dimensional self-organisation of the nanoparticles into supraparticle aggregates. The surface curvature of the component nanoparticles, even the mild curvature associated with 30 nm-diameter particle size, promotes strong contacting of chains between particles, which softens the interaction potential.

Although the collective driving force for formation of particle–particle interfaces is very high in vacuum and so the overall shapes of the assembled supraparticles are determined by kinetics, the softness of the local chain–chain potentials retains self-healing at the molecular scale. The large 30 nm particles thus exhibit an unusual mix of nanoscale thermodynamic and mesoscale kinetic governance.

The results from this study further emphasize the importance of individually-weak intermolecular forces between nanoparticles and surfaces coated with alkanethiol molecules. Indeed, such forces

play a significant role in any systems involving organic molecules, often dominating the conformation of assemblies of monolayers, bilayers and nanofibers.^{62–64} However, we note that the energetic data reported in this work is based on simple binding energies calculated from interaction potential energies over a finite range of pre-defined interaction distances in vacuum. More detailed simulations will be used to calculate the free energy (enthalpic and entropic effects) of the interactions by computing the potential of mean force associated with the binding process in various solvents. The conformations identified in the present work will provide the required starting structures for these calculations together with an expected upper limit on the cohesive strengths (and hence supraparticle porosity) that may be obtained. Modelling of colloidal assemblies using complementary approaches such as DLVO theory^{65–67} would also be useful, particularly for applications which seek to replace the hydrophobic alkyl coats with more polar molecules.

The main prediction from this modelling study is that large 30 nm particles can aggregate into kinetically-stable porous supraparticles, under vacuum conditions and perhaps in solution phase using solvents that aid rather than hamper contacts between nanoparticles. We hope that the data will contribute towards the atomic scale engineering of coated nanoparticles with highly-controllable size, shape and electronic properties⁶⁸ that can be exploited for the creation of ordered meso and macro scale three-dimensional architectures. Deeper understanding of the atomic scale features of the interfaces, and the corresponding meso scale pattern formation,⁶⁹ will aid efforts to design novel macroscopic functional architectures^{70–73} with physicochemical properties tailored for specific device applications, that exploit the coordinative ability (and perhaps pore-building properties) of the individual nanoparticle building blocks.

Acknowledgements

We acknowledge support for this research from the European Community's Seventh Framework Programme (FP7/2007–2013) under grant agreement number 213382 (FUNMOL). DT acknowledges also Science Foundation Ireland (SFI) for financial support under Grant Number 11/SIRG/B2111 and provision of computing resources at Tyndall National Institute, and thanks SFI/Higher Education Authority for computing time at the Irish Centre for High-End Computing (ICHEC). PS acknowledges support by the Foundation for Polish Science (FNP) through TEAM/2010-6/2 project co-financed by the EU European Regional Development Fund. MC acknowledges support from the Innovative Economy grant number POIG.01.01.02.00-008/08 and Polish National Science Centre Grant No. 2011/01/B/ST3/02190.

Notes and references

- M. P. Pileni, *Nat. Mater.*, 2003, **2**, 145–150.
- C. Sanchez, B. Julian, P. Belleville and M. Popall, *J. Mater. Chem.*, 2005, **15**, 3559–3592.
- M. P. Pileni, Y. Lalatonne, D. Ingert, I. Lisiecki and A. Courty, *Faraday Discuss.*, 2004, **125**, 251–264.
- M. P. Pileni, *Nanocrystals forming mesoscopic structures*, Wiley-VCH, John Wiley distributor, Weinheim, Chichester, 2005.
- A. Haryono and W. H. Binder, *Small*, 2006, **2**, 600–611.
- J. B. Pelka, M. Brust, P. Gierlowski, W. Paszkowicz and N. Schell, *Appl. Phys. Lett.*, 2006, **89**, 063110.
- I. Lisiecki, D. Parker, C. Salzemann and M. P. Pileni, *Chem. Mater.*, 2007, **19**, 4030–4036.
- V. Prasad, D. Semwogerere and E. R. Weeks, *J. Phys.: Condens. Matter*, 2007, **19**, 113102.
- I. Lisiecki, M. Walls, D. Parker and M. P. Pileni, *Langmuir*, 2008, **24**, 4295–4299.
- I. Lisiecki and M. P. Pileni, *C. R. Chim.*, 2009, **12**, 235–246.
- I. Lisiecki, S. Turner, S. Bals, M. P. Pileni and G. Van Tendeloo, *Chem. Mater.*, 2009, **21**, 2335–2338.
- D. Y. Wang, *Phys. Chem. Chem. Phys.*, 2010, **12**, 11819–11820.
- Y. S. Xia, T. D. Nguyen, M. Yang, B. Lee, A. Santos, P. Podsiadlo, Z. Y. Tang, S. C. Glotzer and N. A. Kotov, *Nat. Nanotechnol.*, 2011, **6**, 580–587.
- Y. Lalatonne, J. Richardi and M. P. Pileni, *Nat. Mater.*, 2004, **3**, 121–125.
- P. K. Ghorai and S. C. Glotzer, *J. Phys. Chem. C*, 2007, **111**, 15857–15862.
- Y. Qin and K. A. Fichtorn, *J. Chem. Phys.*, 2007, **127**, 144911.
- P. Schapotschnikow and T. J. H. Vlugt, *J. Chem. Phys.*, 2009, **131**, 124705.
- Q. H. Zeng, A. B. Yu and G. Q. Lu, *Ind. Eng. Chem. Res.*, 2010, **49**, 12793–12797.
- C. K. Lee and C. C. Hua, *J. Chem. Phys.*, 2010, **132**, 224904.
- J. H. Liao, M. A. Mangold, S. Grunder, M. Mayor, C. Schonenberger and M. Calame, *New J. Phys.*, 2008, **10**, 065019.
- I. Engquist, I. Lundstrom and B. Liedberg, *J. Phys. Chem.*, 1995, **99**, 12257–12267.
- V. Santhanam and R. P. Andres, *Nano Lett.*, 2004, **4**, 41–44.
- P. L. Silvestrelli, F. Ancilotto, F. Toigo, C. Sbraccia, T. Ikeda and M. Boero, *ChemPhysChem*, 2005, **6**, 1889–1893.
- L. F. Zhang, L. Hong, Y. Yu, S. C. Bae and S. Granick, *J. Am. Chem. Soc.*, 2006, **128**, 9026–9027.
- Y. Li, X. Chen and N. Gu, *J. Phys. Chem. B*, 2008, **112**, 16647–16653.
- P. Schapotschnikow and T. J. H. Vlugt, *J. Phys. Chem. C*, 2010, **114**, 2531–2537.
- P. Schapotschnikow, R. Pool and T. J. H. Vlugt, *Nano Lett.*, 2008, **8**, 2930–2934.
- J. Q. Lin, H. W. Zhang, Z. Chen, Y. G. Zheng, Z. Q. Zhang and H. F. Ye, *J. Phys. Chem. C*, 2011, **115**, 18991–18998.
- O. C. Compton and F. E. Osterloh, *J. Am. Chem. Soc.*, 2007, **129**, 7793–7798.
- N. Goubet, Y. Ding, M. Brust, Z. L. Wang and M. P. Pileni, *ACS Nano*, 2009, **3**, 3622–3628.
- B. Roux, *Comput. Phys. Commun.*, 1995, **91**, 275–282.
- M. Sprik and G. Ciccotti, *J. Chem. Phys.*, 1998, **109**, 7737–7744.
- W. D. Luedtke and U. Landman, *J. Phys. Chem. B*, 1998, **102**, 6566–6572.

- 34 J. C. Love, L. A. Estroff, J. K. Kriebel, R. G. Nuzzo and G. M. Whitesides, *Chem. Rev.*, 2005, **105**, 1103–1169.
- 35 P. Fenter, P. Eisenberger and K. S. Liang, *Phys. Rev. Lett.*, 1993, **70**, 2447–2450.
- 36 G. Gannon, J. A. Larsson, J. C. Greer and D. Thompson, *Langmuir*, 2009, **25**, 242–247.
- 37 J. C. Phillips, R. Braun, W. Wang, J. Gumbart, E. Tajkhorshid, E. Villa, C. Chipot, R. D. Skeel, L. Kale and K. Schulten, *J. Comput. Chem.*, 2005, **26**, 1781–1802.
- 38 A. D. MacKerell, D. Bashford, M. Bellott, R. L. Dunbrack, J. D. Evanseck, M. J. Field, S. Fischer, J. Gao, H. Guo, S. Ha, D. Joseph-McCarthy, L. Kuchnir, K. Kuczera, F. T. K. Lau, C. Mattos, S. Michnick, T. Ngo, D. T. Nguyen, B. Prodhom, W. E. Reiher, B. Roux, M. Schlenkrich, J. C. Smith, R. Stote, J. Straub, M. Watanabe, J. Wiorcikiewicz-Kuczera, D. Yin and M. Karplus, *J. Phys. Chem. B*, 1998, **102**, 3586–3616.
- 39 J. P. Ryckaert, G. Ciccotti and H. J. C. Berendsen, *J. Comput. Phys.*, 1977, **23**, 327–341.
- 40 W. Humphrey, A. Dalke and K. Schulten, *J. Mol. Graphics*, 1996, **14**, 33–38.
- 41 D. L. Ermak and J. A. McCammon, *J. Chem. Phys.*, 1978, **69**, 1352–1360.
- 42 J. C. Wang, P. Neogi and D. Forciniti, *J. Chem. Phys.*, 2006, **125**, 194717.
- 43 J. N. Israelachvili, *Intermolecular and surface forces*, Academic Press, Amsterdam, Waltham, MA, 2011.
- 44 U. Seifert, J. Shillcock and P. Nelson, *Phys. Rev. Lett.*, 1996, **77**, 5237–5240.
- 45 G. Gannon, J. C. Greer, J. A. Larsson and D. Thompson, *ACS Nano*, 2010, **4**, 921–932.
- 46 M. Cieplak and D. Thompson, *J. Chem. Phys.*, 2008, **128**, 234906.
- 47 M. Sikora, P. Szymczak, D. Thompson and M. Cieplak, *Nanotechnology*, 2011, **22**, 445601.
- 48 P. Galvin, D. Thompson, K. B. Ryan, A. McCarthy, A. C. Moore, C. S. Burke, M. Dyson, B. D. MacCraith, Y. K. Gun'ko, M. T. Byrne, Y. Volkov, C. Keely, E. Keehan, M. Howe, C. Duffy and R. MacLoughlin, *Cell. Mol. Life Sci.*, 2012, **69**, 389–404.
- 49 R. A. Rippel and A. M. Seifalian, *J. Nanosci. Nanotechnol.*, 2011, **11**, 3740–3748.
- 50 A. Ulman, *Chem. Rev.*, 1996, **96**, 1533–1554.
- 51 A. Badia, L. Cuccia, L. Demers, F. Morin and R. B. Lennox, *J. Am. Chem. Soc.*, 1997, **119**, 2682–2692.
- 52 J. Fink, C. J. Kiely, D. Bethell and D. J. Schiffrin, *Chem. Mater.*, 1998, **10**, 922–926.
- 53 Z. L. Wang, S. A. Harfenist, R. L. Whetten, J. Bentley and N. D. Evans, *J. Phys. Chem. B*, 1998, **102**, 3068–3072.
- 54 M. P. Pileni, *J. Phys. Chem. B*, 2001, **105**, 3358–3371.
- 55 V. F. Puentes, K. M. Krishnan and A. P. Alivisatos, *Science*, 2001, **291**, 2115–2117.
- 56 M. C. Daniel and D. Astruc, *Chem. Rev.*, 2004, **104**, 293–346.
- 57 J. Liao, L. Bernard, M. Langer, C. Schonenberger and M. Calame, *Adv. Mater.*, 2006, **18**, 2444–2447.
- 58 L. Bernard, Y. Kamdzhilov, M. Calame, S. J. van der Molen, J. H. Liao and C. Schonenberger, *J. Phys. Chem. C*, 2007, **111**, 18445–18450.
- 59 Q. B. Zhang, J. P. Xie, J. Liang and J. Y. Lee, *Adv. Funct. Mater.*, 2009, **19**, 1387–1398.
- 60 M. L. Curri, R. Comparelli, M. Striccoli and A. Agostiano, *Phys. Chem. Chem. Phys.*, 2010, **12**, 11197–11207.
- 61 P. H. Qiu, C. Jensen, N. Charity, R. Towner and C. B. Mao, *J. Am. Chem. Soc.*, 2010, **132**, 17724–17732.
- 62 G. Gannon, C. O'Dwyer, J. A. Larsson and D. Thompson, *J. Phys. Chem. B*, 2011, **115**, 14518–14525.
- 63 C. O'Dwyer, G. Gannon, D. McNulty, D. N. Buckley and D. Thompson, *Chem. Mater.*, 2012, **24**, 3981–3992.
- 64 N. Nerngchamnon, Y. Li, D. Qi, L. Jian, D. Thompson and C. A. Nijhuis, *Nat. Nanotechnol.*, 2013, **8**, 113–118.
- 65 E. M. Hotze, T. Phenrat and G. V. Lowry, *J. Environ. Qual.*, 2010, **39**, 1909–1924.
- 66 T. Ederth, *J. Phys. Chem. B*, 2000, **104**, 9704–9712.
- 67 J. Wang and R.-H. Yoon, *Langmuir*, 2008, **24**, 7889–7896.
- 68 D. Thompson, J. P. Hermes, A. J. Quinn and M. Mayor, *ACS Nano*, 2012, **6**, 3007–3017.
- 69 S. J. Khan, F. Pierce, C. M. Sorensen and A. Chakrabarti, *Langmuir*, 2009, **25**, 13861–13868.
- 70 A. Terfort, N. Bowden and G. M. Whitesides, *Nature*, 1997, **386**, 162–164.
- 71 J. Lahann, S. Mitragotri, T. N. Tran, H. Kaido, J. Sundaram, I. S. Choi, S. Hoffer, G. A. Somorjai and R. Langer, *Science*, 2003, **299**, 371–374.
- 72 H. F. Yu, T. Iyoda and T. Ikeda, *J. Am. Chem. Soc.*, 2006, **128**, 11010–11011.
- 73 A. Harada, R. Kobayashi, Y. Takashima, A. Hashidzume and H. Yamaguchi, *Nat. Chem.*, 2011, **3**, 34–37.